

# Light-Induced Valleytronics in Pristine Graphene

M. S. Mrudul,<sup>1</sup> Álvaro Jiménez-Galán,<sup>2</sup> Misha Ivanov,<sup>2</sup> and Gopal Dixit<sup>1,\*</sup>

<sup>1</sup>*Department of Physics, Indian Institute of  
Technology Bombay, Powai, Mumbai 400076, India*

<sup>2</sup>*Max-Born Institut, Max-Born Straße 2A, 12489 Berlin, Germany*

(Dated: March 19, 2021)

## Abstract

Electrons in two-dimensional hexagonal materials have valley degree of freedom, which can be used to encode and process quantum information. The valley-selective excitations, governed by the circularly polarised light resonant with the material's band-gap, continues to be the foundation of valleytronics. It is often assumed that achieving valley selective excitation in pristine graphene with all-optical means is not possible due to the inversion symmetry of the system. Here we demonstrate that both valley-selective excitation and valley-selective high-harmonic generation can be achieved in pristine graphene by using the combination of two counter-rotating circularly polarized fields, the fundamental and its second harmonic. Controlling the relative phase between the two colours allows us to select the valleys where the electron-hole pairs and higher-order harmonics are generated. We also describe an all-optical method for measuring valley polarization in graphene with a weak probe pulse. This work offers a robust recipe to write and read valley-selective electron excitations in materials with zero bandgap and zero Berry curvature.

---

\* [gdixit@phy.iitb.ac.in](mailto:gdixit@phy.iitb.ac.in)

The realisation of atomically-thin monolayer graphene has led to breakthroughs in fundamental and applied sciences [1, 2]. Charge carriers in graphene are described by the massless Dirac equation and exhibit exceptional transport properties [3], making graphene very attractive for novel electronics applications. One of the most interesting features of graphene and gapped graphene materials is the electron’s extra degree of freedom, the valley pseudospin, associated with populating the local minima  $\mathbf{K}$  and  $\mathbf{K}'$  in the lowest conduction band of the Brillouin zone. This extra degree of freedom has the potential to encode, process and store quantum information, opening the field of valleytronics [4].

The monolayer graphene, as opposed to gapped graphene materials, presents a fundamental challenge for valleytronics: it has zero bandgap and zero Berry curvature. These aspects are generally considered to be a major impediment for valleytronics. In gapped graphene materials, valley selectivity is achieved by matching the helicity of a circularly polarized pump pulse, resonant to the bandgap, to the sign of the Berry curvature [5–9]. Recently demonstrated [10] sub-cycle manipulation of electron population in  $\mathbf{K}$  and  $\mathbf{K}'$  valleys of tungsten diselenide, achieved with the combination of a resonant pump pulse locked to the oscillations of the THz control pulse, represents a major milestone. Precise sub-cycle control over the driving light fields opens new opportunities for valleytronics, such as those offered by the new concept of a topological resonance, discovered and analysed in Refs. [11–13]. Single-cycle pulses with the controlled phase of carrier oscillations under the envelope offer a route to valleytronics in gapped graphene-type materials even when such pulses are linearly, not circularly, polarized [14]. It is also possible to avoid the reliance on resonances in gapped graphene-type materials, breaking the symmetry between the  $\mathbf{K}$  and  $\mathbf{K}'$  valleys via a light-induced topological phase transition, closing the gap in the desired valley [15].

Thus, with its zero bandgap, zero Berry curvature, and identical dispersion near the bottom of the valleys, pristine graphene appears unsuitable for valleytronics – a disappointing conclusion in view of its exceptional transport properties. We show that this generally accepted conclusion is not correct, and that the preferential population of a desired valley can be achieved by tailoring the polarization state of the driving light pulse to the symmetry of the lattice. Our proposal offers an all-optical route to valleytronics in pristine graphene, complementing approaches based on creating a gap by using a heterostructure of graphene with hexagonal boron nitride [16–19], or by adding strain and/or defect engineering [20–24].

While light configuration we use is similar to that used in Ref. [15] for finite bandgap

materials, the physical mechanism underlying valley-selective excitation in a zero-band-gap, centrosymmetric material such as graphene is quite different. In gapped materials, valley polarization is achieved by selectively reducing the effective bandgap in one of the valleys [15]. Here, valley polarization is achieved only when the light-driven electrons explore the anisotropic region in the Brillouin zone.

We also show valley selectivity of harmonic generation in graphene, and demonstrate it with the same field as we use for valley-selective electronic excitation. High-harmonic generation (HHG) is a powerful method for probing attosecond electron dynamics in systems as diverse as atoms, molecules [25–30] and solids [31–44]. In solids, high harmonic spectroscopy was used to probe valence electrons [35], atomic arrangement in solids [35–37], defects [45, 46], band dispersion [38–40] and quantum phase transitions [41, 42, 47], and to realise petahertz electronics in solids [35, 43, 44]. Last but not least, we describe an all-optical method for measuring valley polarization in graphene with a weak probe pulse.

The key idea of our approach is illustrated in Fig. 1, which shows graphene in real (a) and reciprocal (b) space, together with the structure of the incident electric field (a) and the corresponding vector potential (b). The field is made by superimposing two counter-rotating circularly polarized colours at the frequencies  $\omega$  and  $2\omega$ . The Lissajous figure for the total electric field is a trefoil, and its orientation is controlled by the relative two-colour phase  $\phi$ , i.e., the sub-cycle two-colour delay measured in terms of  $\omega$ . In the absence of the field, the two carbon atoms A and B, in real space, are related by the inversion symmetry. When the field is turned on, this inversion symmetry is broken: the electric field in panel (a) always points from the atom A to the one of the three neighbouring atoms B during the full laser cycle, but not the other way around. Indeed, if the centre of the Lissajous figure is placed on the atom B, the field points in the middle between its neighbours. One can control this symmetry breaking by rotating the trefoil, interchanging the roles of the atoms A and B. Thus, the bi-circular field offers simple, all-optical, ultrafast tool to break the inversion symmetry of the graphene lattice in a controlled way. Such controlled symmetry breaking allows one to control the relative excitation probabilities induced by the same laser field in the adjacent  $\mathbf{K}$  and  $\mathbf{K}'$  valleys of the Brillouin zone.

Panel (b) provides the complementary reciprocal-space perspective. In the laser field, the electron crystal momentum follows  $\mathbf{k}(t) = \mathbf{k}_i + \mathbf{A}(t)$ , where  $\mathbf{k}_i$  is the initial crystal momentum and  $\mathbf{A}(t)$  is the laser vector potential, shown in (b) for the electric field shown

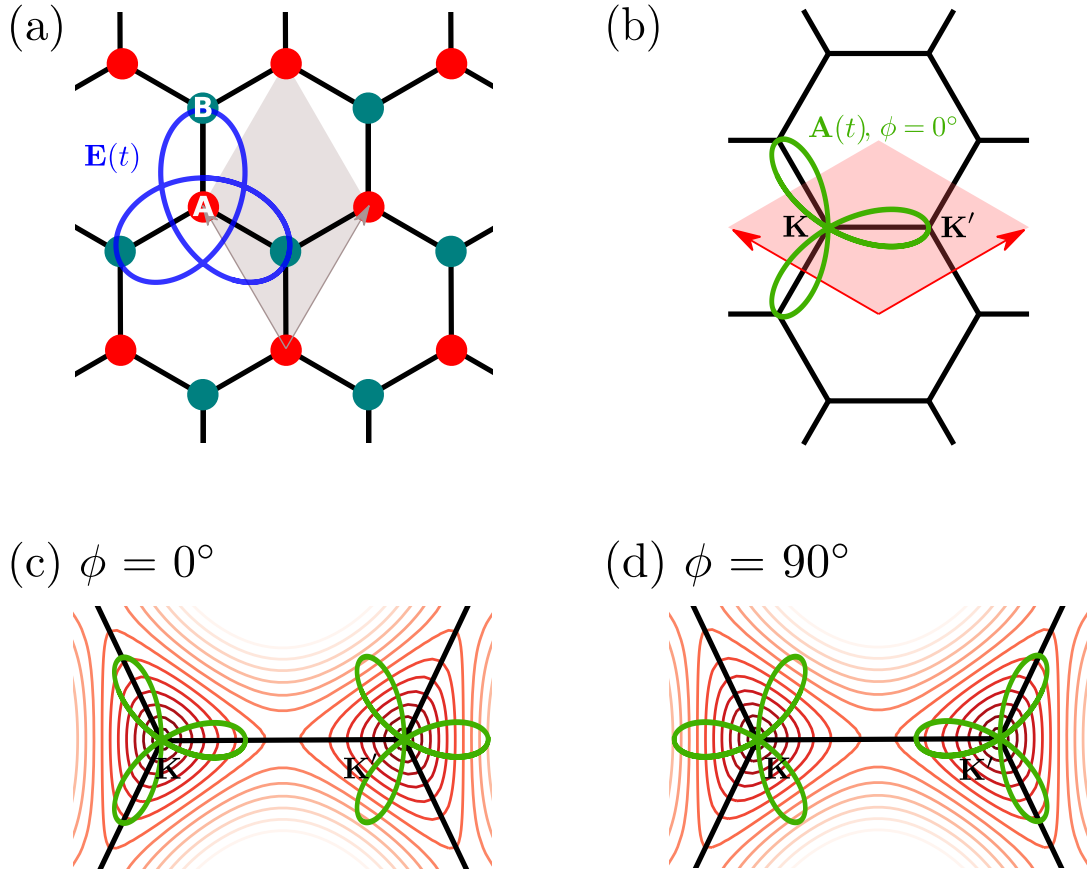


FIG. 1. Physical mechanism of valley polarization in graphene. (a) Graphene lattice in the coordinate space, with the Lissajous figure of the bicircular electric field breaking the symmetry between otherwise identical carbon atoms A and B; two-colour phase  $\phi = 0$ . (b) Optically induced symmetry breaking viewed in the momentum space, the vector potential of the bicircular field is shown for  $\phi = 0$ . (c, d) Close-up images of the valleys show their asymmetry, leading to different laser-driven dynamics and different excitation rates once the electron leaves the bottom of the valley. Here, the red contours show the conduction band energy in the reciprocal space.

in (a). The asymmetry between the two valleys with respect to the vector potential is immediately visible.

Panels (c) and (d) provide additional support to this qualitative picture. One can observe that the two field-free valleys,  $\mathbf{K}$  and  $\mathbf{K}'$ , are only identical near their very bottoms. As soon as one moves away from the bottom, the valleys start to develop the trefoil structure, with  $\mathbf{K}$  and  $\mathbf{K}'$  being the mirror images of each other. How the symmetry of the vector potential

fits into the symmetry of the valley away from their bottoms will control the dynamics and the excitation probability.

In sufficiently strong fields, excitation happens not only at the Dirac point where the gap is equal to zero, but also in its vicinity. For the vector potential in panel (c), the average gap seen by the electron when following the vector potential from the Dirac point in the  $\mathbf{K}$  valley, i.e., moving along the trajectory  $\mathbf{K} + \mathbf{A}(t)$ , is less than in the  $\mathbf{K}'$  valley, i.e., when following the trajectory  $\mathbf{K}' + \mathbf{A}(t)$ . In sufficiently strong and low-frequency fields, such that the bandgap along the trajectories  $\mathbf{K} + \mathbf{A}(t)$  and  $\mathbf{K}' + \mathbf{A}(t)$  quickly exceeds the photon energy, the excitation probability should be higher in panel (c). For the same reason, rotating the vector potential as shown in panel (d) should favour population of the  $\mathbf{K}'$  valley. Here, “quickly” means “within a fraction of one-third of the laser cycle”, which is the relevant time-scale for the bi-circular field. In this context, lower laser frequencies leading to higher vector potential are better suited to meet this requirement.

In the simulations, we used the nearest-neighbour tight-binding approximation to obtain the ground state of graphene with a hopping-energy of 2.7 eV [48]. The lattice parameter of graphene is chosen to be 2.46 Å. The resultant band-structure has zero band-gap with linear dispersion near the two points in the Brillouin zone known as  $\mathbf{K}$  and  $\mathbf{K}'$  points.

The density matrix approach was used to follow the electron dynamics in graphene. Time-evolution of density matrix element,  $\rho_{mn}^{\mathbf{k}}$ , was performed using semiconductor Bloch equations within the Houston basis  $|n, \mathbf{k} + \mathcal{A}(t)\rangle$  as [49, 50]

$$\partial_t \rho_{mn}^{\mathbf{k}} = -i\epsilon_{mn}^{\mathbf{k}+\mathcal{A}(t)} \rho_{mn}^{\mathbf{k}} - (1 - \delta_{mn}) \frac{\rho_{mn}^{\mathbf{k}}}{T_2} + i\mathcal{F}(t) \cdot \left[ \sum_l \left( \mathbf{d}_{ml}^{\mathbf{k}+\mathcal{A}(t)} \rho_{ln}^{\mathbf{k}} - \mathbf{d}_{ln}^{\mathbf{k}+\mathcal{A}(t)} \rho_{ml}^{\mathbf{k}} \right) \right]. \quad (1)$$

Here,  $\epsilon_{mn}^{\mathbf{k}}$  and  $\mathbf{d}_{mn}^{\mathbf{k}}$  are, respectively, the band-gap energy and the dipole-matrix elements between  $m$  and  $n$  energy-bands at  $\mathbf{k}$ . Dipole matrix elements were calculated as  $\mathbf{d}_{mn}^{\mathbf{k}} = -i\langle u_m^{\mathbf{k}} | \nabla_{\mathbf{k}} | u_n^{\mathbf{k}} \rangle$ , where  $u_n^{\mathbf{k}}$  is the periodic part of the Bloch function.  $\mathcal{F}(t)$  and  $\mathcal{A}(t)$  are, respectively, the electric field and vector potential of the laser field and are related as  $\mathcal{F}(t) = -\partial\mathcal{A}(t)/\partial t$ . A phenomenological term accounting for the decoherence is added with a constant dephasing time  $T_2$ . Conduction band population relaxation was neglected [51].

The total current was calculated as

$$\mathbf{J}(\mathbf{k}, t) = \sum_{m,n} \rho_{mn}^{\mathbf{k}}(t) \mathbf{p}_{nm}^{\mathbf{k}+\mathcal{A}(t)}. \quad (2)$$

Here,  $\mathbf{p}_{nm}^{\mathbf{k}}$  are the momentum matrix elements, obtained as  $\mathbf{p}_{nm}^{\mathbf{k}} = \langle n, \mathbf{k} | \nabla_{\mathbf{k}} \hat{H}_{\mathbf{k}} | m, \mathbf{k} \rangle$ . The off-diagonal elements of momentum and dipole-matrix elements are related as  $\mathbf{d}_{mn}^{\mathbf{k}} = i\mathbf{p}_{mn}^{\mathbf{k}}/\epsilon_{mn}^{\mathbf{k}}$ .

Finally, the harmonic spectrum was determined from the Fourier-transform of the time-derivative of the total current as

$$\mathcal{I}(\omega) = \left| \mathcal{FT} \left( \frac{d}{dt} \left[ \int_{BZ} \mathbf{J}(\mathbf{k}, t) d\mathbf{k} \right] \right) \right|^2. \quad (3)$$

Here, integration is performed over the entire Brillouin zone.

Valley-selective electronic excitation induced by the tailored field is confirmed by our numerical simulations. In the simulations, graphene is exposed to the bicircular field with the vector potential

$$\mathcal{A}(t) = \frac{A_0 f(t)}{\sqrt{2}} \left( \left[ \cos(\omega t + \phi) + \frac{\mathcal{R}}{2} \cos(2\omega t) \right] \hat{\mathbf{e}}_x + \left[ \sin(\omega t + \phi) - \frac{\mathcal{R}}{2} \sin(2\omega t) \right] \hat{\mathbf{e}}_y \right). \quad (4)$$

Here,  $A_0 = F_\omega/\omega$  is the amplitude of the vector potential for the fundamental field,  $F_\omega$  is its strength,  $f(t)$  is the temporal envelope of the driving field,  $\phi$  is the sub-cycle phase difference between the two fields, and  $\mathcal{R}$  is the ratio of the electric field strengths for the two fields, leading to  $\mathcal{R}/2$  ratio for the amplitudes of the vector potentials. The amplitude of the fundamental field was varied up to  $F_\omega = 15$  MV/cm, leading to the maximum fundamental intensity  $3 \times 10^{11}$  W/cm<sup>2</sup>, with the fundamental wavelength  $\lambda = 6\mu\text{m}$ . This laser intensity is below the damage threshold for the monolayer graphene [52–54]. We have also varied  $\mathcal{R}$ , using  $\mathcal{R} = 1$  and  $\mathcal{R} = 2$ . A pulse with sin-squared envelope and 145 femtosecond duration (zero-to-zero) is employed in this work. Our findings are valid for a broad range of wavelengths and field intensities. To obtain the total population of the different valleys, we have integrated the momentum-resolved population over the sections shown in Fig. 2(a).

To quantify the amount of the valley polarisation, we used the valley asymmetry parameter defined as

$$\eta = \frac{n_c^{\mathbf{K}'} - n_c^{\mathbf{K}}}{(n_c^{\mathbf{K}'} + n_c^{\mathbf{K}})/2}, \quad (5)$$

where  $n_c^{\mathbf{K}'}$  and  $n_c^{\mathbf{K}}$  are electron populations at the end of the laser pulse in the conduction band around  $\mathbf{K}'$  and  $\mathbf{K}$  valleys, respectively.

Fig. 2(b) shows the asymmetry in the populations of the  $\mathbf{K}$  and  $\mathbf{K}'$  valleys as a function of the two-colour phase  $\phi$ , for several values of the fundamental field amplitude and  $\mathcal{R} = 2$ .

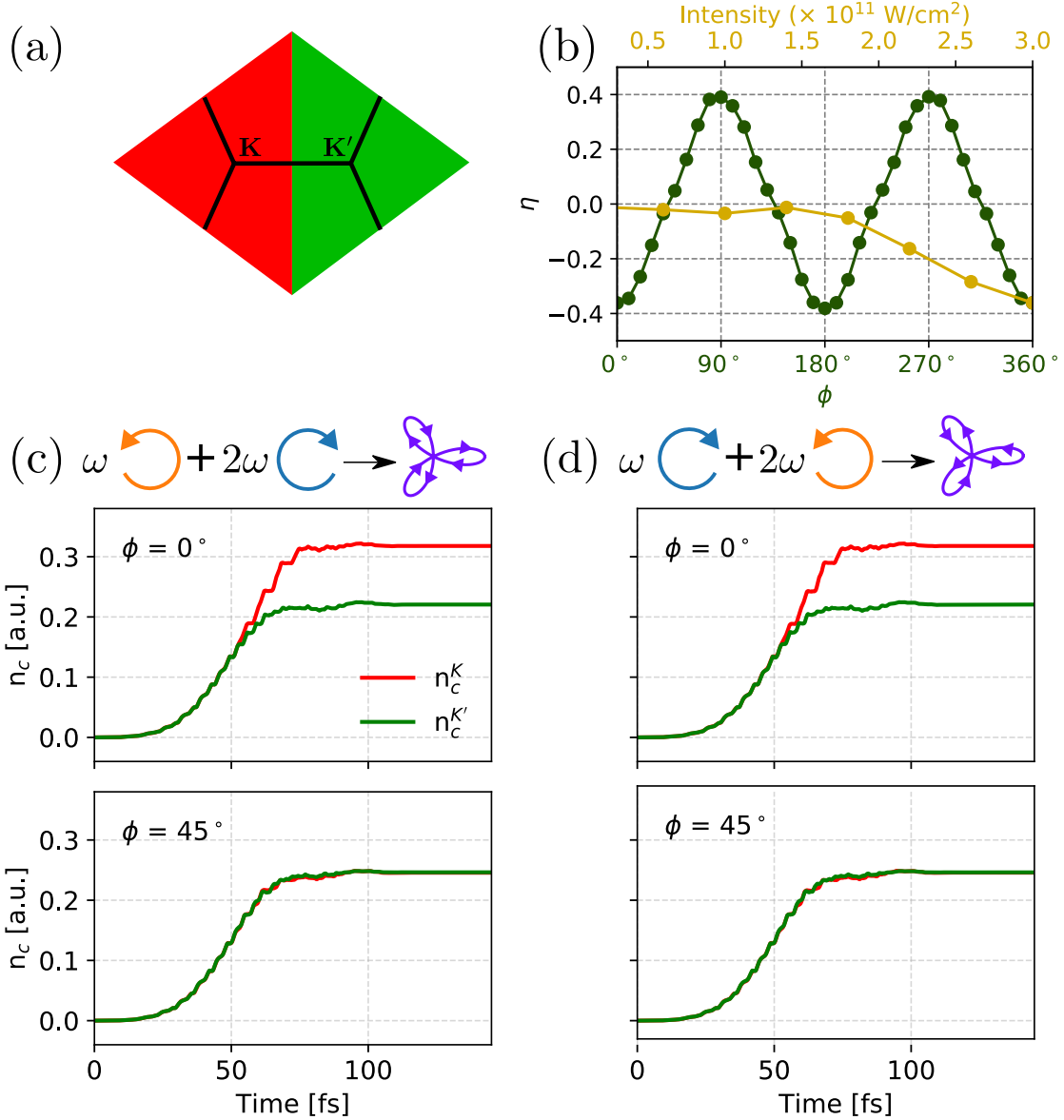


FIG. 2. Valley asymmetry around two valleys  $\mathbf{K}'$  and  $\mathbf{K}$ . (a) Separation of the Brillouin zone into the  $\mathbf{K}'$  and  $\mathbf{K}$  valleys. (b) Asymmetry in the valley-resolved populations in the conduction band as a function of  $\phi$  (green line with an intensity  $3 \times 10^{11} \text{ W/cm}^2$ ), and laser intensity (yellow line with  $\phi = 0^\circ$ ) for a laser with wavelength of  $6 \mu\text{m}$ ,  $\mathcal{R} = 2$ , and a dephasing time of  $10 \text{ fs}$ . (c, d) Excitation dynamics during the laser pulse for  $\phi = 0^\circ, 45^\circ$ : switching the helicities of both the fields simultaneously does not change the outcome.

Substantial contrast between the two valleys is achieved once the excitations leave the bottom of the Dirac cone, with values as high as  $\pm 36\%$  for  $\phi = 0^\circ, 90^\circ$ , and no asymmetry at  $\phi = 45^\circ$ . Here, each  $180^\circ$  change in  $\phi$  results in  $120^\circ$  rotation of the trefoil, yielding an

equivalent configuration. This is the reason for the periodicity of the valley asymmetry presented in Fig. 2(b). The higher-populated valley is the one where the vector potential “fits” better into the shape of the valley, minimizing the bandgap along the electron trajectory in the momentum space. The same results are obtained when simultaneously changing the helicities of both driving fields, Fig. 2(c, d). The asymmetry in the valley population is negligible up to an intensity of  $2 \times 10^{11}$  W/cm<sup>2</sup> and gradually increases with intensity [Fig. 2 (b)]. This shows that the valley asymmetry is observed only when the laser pulse is able to drive the electrons to the anisotropic part of the conduction band.

The current generated by the electron injection into the conduction band valleys is accompanied by harmonic radiation and makes substantial contribution to the lower order harmonics, such as H4 and H5 for our two-colour driver. These harmonics are stronger whenever the dispersion  $\epsilon(\mathbf{k})$  is more nonlinear. In this respect, for the electrons following the trajectories  $\mathbf{K} + \mathbf{A}(t)$  and  $\mathbf{K}' + \mathbf{A}(t)$ , the current-driven high harmonic generation from the  $\mathbf{K}'$  valley is preferred for the vector potential in Fig. 1(c). Conversely, for the vector potential in Fig. 1(d) low-order, current-driven harmonic generation should be preferred from the  $\mathbf{K}$  valley. Indeed, following the vector potential, the electron is driven against the steeper walls in the  $\mathbf{K}'$  valley in panel (c) and against the steeper walls in the  $\mathbf{K}$  valley in panel (d).

These qualitative expectations are also confirmed by our numerical simulations, shown in Fig. 3. The same laser parameters used in Fig. 2 are used in this simulation.

In general, the interband and intraband harmonic emission mechanisms in graphene are coupled [55–57], except at low electric fields [57], leading to a complex interplay between the interband and intraband emission mechanisms. The former should be more sensitive to the dephasing than the latter. To this end, we have calculated the the harmonic spectrum for different dephasing times  $T_2$ , see Fig. 3(a). We find that the harmonic emission is essentially  $T_2$ -independent, until at least H13, suggesting that the intraband emission mechanism is generally dominant.

Fig. 3(b) shows polarisation-resolved high-harmonic spectrum. The  $(3n + 1)$  harmonics follow the polarisation of the  $\omega$  pulse (left-handed circular polarisation), whereas  $(3n + 2)$  harmonics follow the polarisation of the  $2\omega$  pulse (right-handed circular polarisation), while  $3n$  harmonics are missing, just like in atomic media [58, 59]. In this context, we note that while harmonic generation with single-colour circularly polarized drivers is forbidden



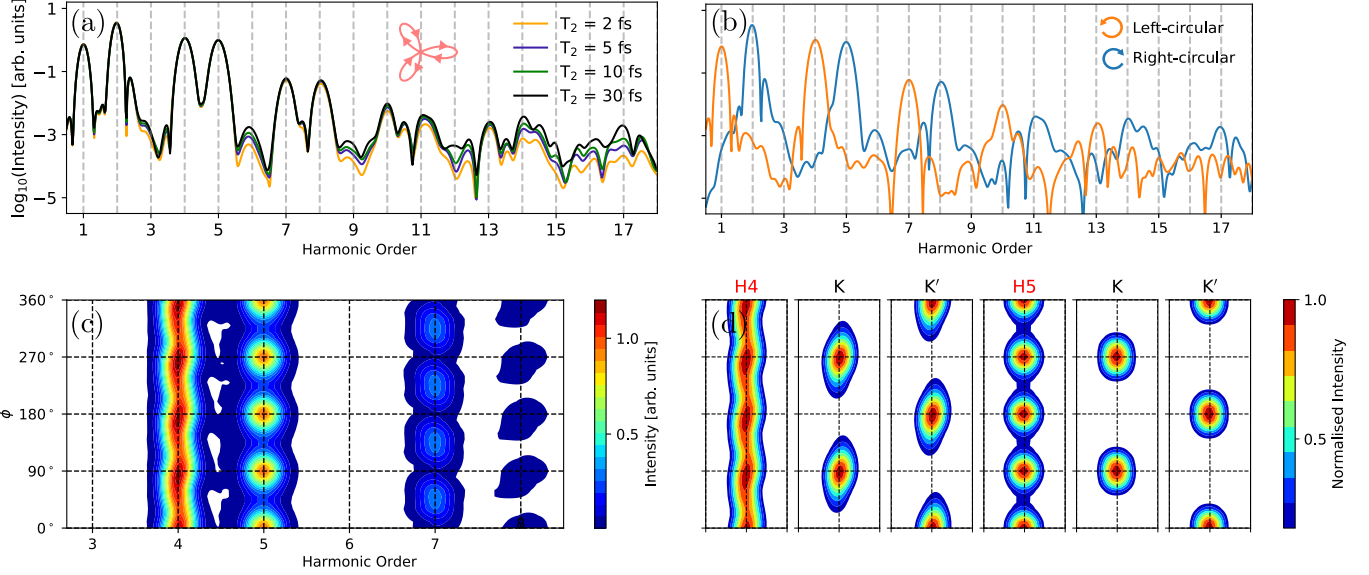


FIG. 3. Valley polarization in high-harmonic emission driven by a bicircular field in graphene. (a) Harmonic spectrum for different dephasing times, for the vector potential shown in the inset ( $\phi = 0$ ); (b) Polarisation-resolved high harmonic emission, for left-handed circularly polarised fundamental (orange) and right-handed circularly polarised second harmonic (blue). Alternating harmonics follow alternating helicities:  $3n + 1$  follow the fundamental,  $3n + 2$  follow the second harmonic, the  $3n$  harmonics missing due to symmetry. (c) Harmonic emission as a function of the two-colour phase  $\phi$ . (d) Valley polarization of H4 and H5 as a function of the two-colour phase. The total field is identical for  $\phi = 0^\circ$  and  $\phi = 180^\circ$  owing to the threefold symmetry.

in atoms, such selection rules do not generally arise in solids [32]. However, the ellipticity-dependence studies on graphene show very weak harmonic yield for drivers with higher ellipticity [52, 55, 56], as we have also observed. As in atoms, application of bicircular fields allows for efficient generation of circularly polarized harmonics in graphene.

Fig. 3(c) shows the dependence of harmonic generation on the orientation of the vector potential relative to the structure of the Brillouin zone. As expected, the total harmonic yield is modulated as the trefoil is rotated, with the lower-order current-driven harmonics H4 and H5 following the expected pattern, maximizing when the electrons are driven into the steeper walls in either the  $\mathbf{K}'$  or  $\mathbf{K}$  valley.

The contribution of different valleys to H4 and H5 as a function of the field orientation is presented in Figs. 3(d). Consistent with the qualitative analysis above, maximum harmonic

contribution of the  $\mathbf{K}'$  valley corresponds to the vector potential orientations such as shown in Fig. 1(c), while the maximum contribution of the  $\mathbf{K}$  valley corresponds to the vector potential orientations such as shown in Fig. 1(d). Therefore, we are able to control the valley-polarisation of the harmonics by controlling the two-colour phase  $\phi$ . We have also checked that these results do not depend on the specific directions of rotation of the two driving fields. That is, we find the same results when simultaneously changing the helicities of both driving fields.

To read-out the induced valley polarization, we employ a probe pulse of frequency  $3\omega$  linearly polarized along the x direction (parallel to  $\Gamma$ - $\mathbf{K}$  and  $\mathbf{K}'$ - $\mathbf{K}$  directions in the Brillouin zone). The amplitude of the probe field is 1.5 MV/cm ( $F_\omega/10$ ). Since the  $\mathbf{K}'$ ,  $\mathbf{K}$  valleys in graphene are related by space inversion, the even-order harmonics generated by individual (asymmetric) valleys are equal in magnitude but opposite in phase, see Fig. 4(a) (red and green lines). In the absence of valley polarization, their interference leads to complete cancellation of even harmonics, Fig. 4(a) (full BZ signal). In the presence of valley polarization, the symmetry is broken, the cancellation of even harmonics is quenched, and even harmonics signal scales proportional to valley polarization (see also [60] and [14]). The phase of the even harmonics follows the dominant valley. Importantly,  $3N\omega$  harmonics are absent in the spectra generated by the bicircular  $\omega - 2\omega$  field, Fig. 3(b). Thus, even harmonics generated by the  $3\omega$  probe provide background-free measurement of valley polarization.

Figure 4(b) shows generation of the second harmonic of the  $3\omega$  probe pulse (labelled H6) for the two-color phases of the bi-circular pump  $\phi = 0^\circ$  (red curve) and  $90^\circ$  (green curve), which switches the valley polarization between  $\mathbf{K}$  and  $\mathbf{K}'$  valleys. While the H6 intensity measures valley polarization, its phase clearly identifies the dominant valley. This phase can be measured by interfering the signal with the reference second harmonic of  $3\omega$  generated, e.g., from a BBO crystal. Controlling the delay of the reference second harmonic generated in the BBO crystal, we can map the phase of H6 generated by graphene on the amplitude modulation of their interference.

In summary, valley polarisation in both electronic excitation and harmonic generation can be achieved in pristine graphene by tailoring the Lissajous figure of the driving pulse to the symmetry of the graphene lattice. This allows one to both break the inversion symmetry between the adjacent carbon atoms and also exploit the anisotropic regions in the valleys, taking advantage of the fact that the energy landscape of the valleys are mirror images

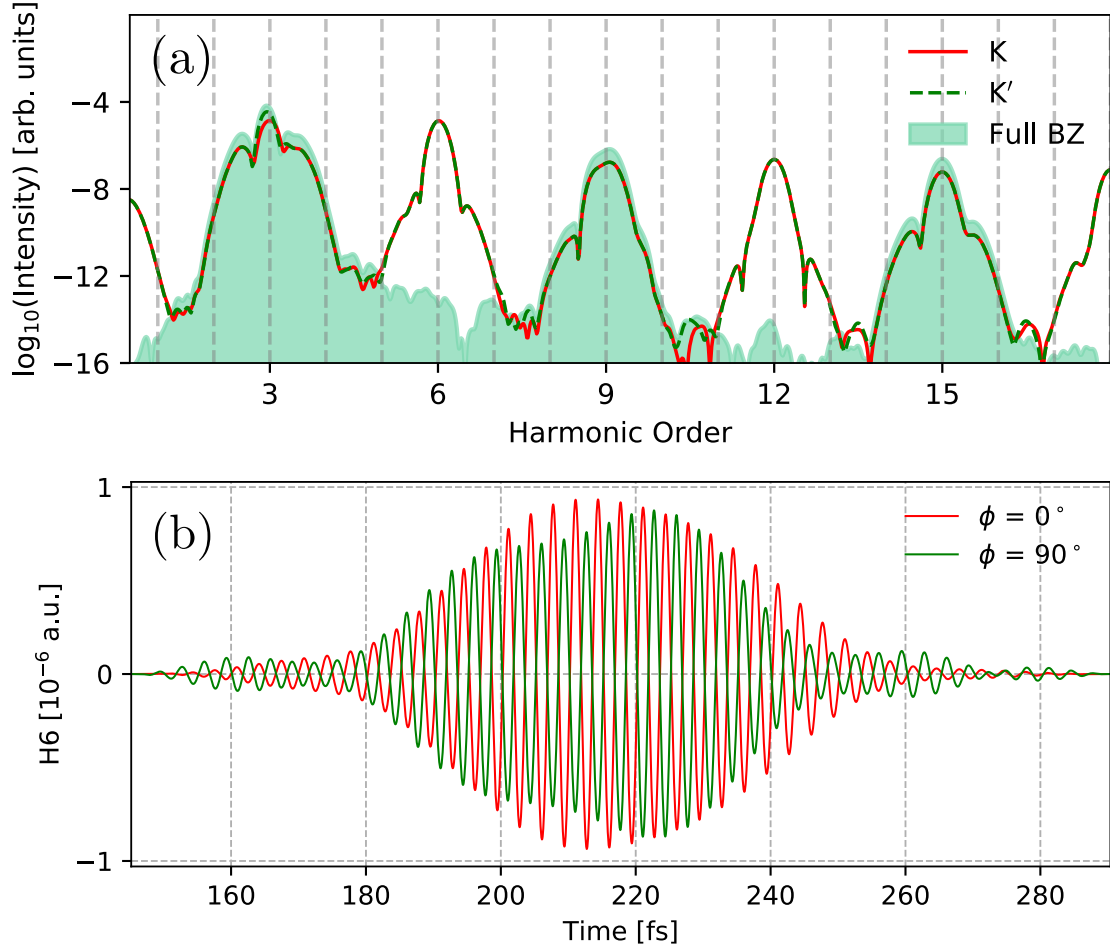


FIG. 4. Read-out of the induced valley-polarization in graphene. (a) Harmonic spectrum corresponding to a linearly polarised field with an amplitude of 1.5 MV/cm and a frequency of  $3\omega$  for monolayer graphene. The red and green lines show the valley-resolved HHG spectrum. (b) The 6<sup>th</sup> harmonic (H6) generated by  $3\omega$  pulse after the bicircular field broke the inversion symmetry in graphene.

of each other. Present work opens an avenue for a new regime of valleytronics in pristine graphene and similar materials with zero bandgap and zero Berry curvature.

## FUNDING

M.I. acknowledges support from the Deutsche Forschungsgemeinschaft (DFG) Quantum Dynamics in Tailored Intense Fields (QUTIF) grant. M.I. and A. J-G acknowledge funding from the European Union's Horizon 2020 research and innovation programme under

grant agreement No 899794, “Optologic.” G. D. acknowledges support from Science and Engineering Research Board (SERB) India (Project No. ECR/2017/001460).

## DISCLOSURES

The authors declare no conflicts of interest.

- 
- [1] Novoselov, K. S. *et al.* Electric field effect in atomically thin carbon films. Science **306**, 666–669 (2004).
  - [2] Geim, A. K. Graphene: status and prospects. Science **324**, 1530–1534 (2009).
  - [3] Neto, A. H. C., Guinea, F., Peres, N. M. R., Novoselov, K. S. & Geim, A. K. The electronic properties of graphene. Reviews of Modern Physics **81**, 109 (2009).
  - [4] Vitale, S. A. *et al.* Valleytronics: opportunities, challenges, and paths forward. Small **14**, 1801483 (2018).
  - [5] Schaibley, J. R. *et al.* Valleytronics in 2d materials. Nature Reviews Materials **1**, 16055 (2016).
  - [6] Mak, K. F., He, K., Shan, J. & Heinz, T. F. Control of valley polarization in monolayer mos2 by optical helicity. Nature Nanotechnology **7**, 494–498 (2012).
  - [7] Jones, A. M. *et al.* Optical generation of excitonic valley coherence in monolayer wse2. Nature Nanotechnology **8**, 634–638 (2013).
  - [8] Gunlycke, D. & White, C. T. Graphene valley filter using a line defect. Physical Review Letters **106**, 136806 (2011).
  - [9] Xiao, D., Liu, G. B., Feng, W., Xu, X. & Yao, W. Coupled spin and valley physics in monolayers of mos 2 and other group-vi dichalcogenides. Physical Review Letters **108**, 196802 (2012).
  - [10] Langer, F. *et al.* Lightwave valleytronics in a monolayer of tungsten diselenide. Nature **557**, 76 (2018).
  - [11] Motlagh, S. A. O., Nematollahi, F., Apalkov, V. & Stockman, M. I. Topological resonance and single-optical-cycle valley polarization in gapped graphene. Physical Review B **100**, 115431 (2019).

- [12] Motlagh, S. A. O., Wu, J. S., Apalkov, V. & Stockman, M. I. Femtosecond valley polarization and topological resonances in transition metal dichalcogenides. Physical Review B **98**, 081406 (2018).
- [13] Kelardeh, H. K., Apalkov, V. & Stockman, M. I. Attosecond strong-field interferometry in graphene: Chirality, singularity, and berry phase. Physical Review B **93**, 155434 (2016).
- [14] Jiménez-Galán, Á., Silva, R., Smirnova, O. & Ivanov, M. Sub-cycle valleytronics: control of valley polarization using few-cycle linearly polarized pulses. Optica **8**, 277–280 (2021).
- [15] Jiménez-Galán, Á., Silva, R. E. F., Smirnova, O. & Ivanov, M. Lightwave control of topological properties in 2d materials for sub-cycle and non-resonant valley manipulation. Nature Photonics **14**, 728–732 (2020).
- [16] Gorbachev, R. V. et al. Detecting topological currents in graphene superlattices. Science **346**, 448–451 (2014).
- [17] Yankowitz, M. et al. Emergence of superlattice dirac points in graphene on hexagonal boron nitride. Nature Physics **8**, 382–386 (2012).
- [18] Hunt, B. et al. Massive dirac fermions and hofstadter butterfly in a van der waals heterostructure. Science **340**, 1427–1430 (2013).
- [19] Rycerz, A., Tworzydło, J. & Beenakker, C. W. J. Valley filter and valley valve in graphene. Nature Physics **3**, 172–175 (2007).
- [20] Grujić, M. M., Tadić, M. Ž. & Peeters, F. M. Spin-valley filtering in strained graphene structures with artificially induced carrier mass and spin-orbit coupling. Physical Review Letters **113**, 046601 (2014).
- [21] Settnes, M., Power, S. R., Brandbyge, M. & Jauho, A. P. Graphene nanobubbles as valley filters and beam splitters. Physical Review Letters **117**, 276801 (2016).
- [22] Faria, D., León, C., Lima, L. R. F., Latgé, A. & Sandler, N. Valley polarization braiding in strained graphene. Physical Review B **101**, 081410 (2020).
- [23] Xiao, D., Yao, W. & Niu, Q. Valley-contrasting physics in graphene: magnetic moment and topological transport. Physical Review Letters **99**, 236809 (2007).
- [24] Rodriguez-Vega, M., Vogl, M. & Fiete, G. A. Floquet engineering of twisted double bilayer graphene. Physical Review Research **2**, 033494 (2020).
- [25] Lein, M. Molecular imaging using recolliding electrons. Journal of Physics B: Atomic, Molecular and Optical Physics **40**, R135 (2007).

- [26] Baker, S. et al. Probing proton dynamics in molecules on an attosecond time scale. Science **312**, 424–427 (2006).
- [27] Smirnova, O. et al. High harmonic interferometry of multi-electron dynamics in molecules. Nature **460**, 972–977 (2009).
- [28] Shafir, D. et al. Resolving the time when an electron exits a tunnelling barrier. Nature **485**, 343–346 (2012).
- [29] Bruner, B. D. et al. Multidimensional high harmonic spectroscopy of polyatomic molecules: detecting sub-cycle laser-driven hole dynamics upon ionization in strong mid-ir laser fields. Faraday discussions **194**, 369–405 (2016).
- [30] Wörner, H. J., Bertrand, J. B., Kartashov, D. V., Corkum, P. B. & Villeneuve, D. M. Following a chemical reaction using high-harmonic interferometry. Nature **466**, 604–607 (2010).
- [31] Kruchinin, S. Y., Krausz, F. & Yakovlev, V. S. Colloquium: Strong-field phenomena in periodic systems. Reviews of Modern Physics **90**, 021002 (2018).
- [32] Ghimire, S. et al. Observation of high-order harmonic generation in a bulk crystal. Nature Physics **7**, 138–141 (2011).
- [33] Schubert, O. et al. Sub-cycle control of terahertz high-harmonic generation by dynamical bloch oscillations. Nature Photonics **8**, 119 (2014).
- [34] Langer, F. et al. Lightwave-driven quasiparticle collisions on a subcycle timescale. Nature **533**, 225 (2016).
- [35] Lakhotia, H. et al. Laser picoscopy of valence electrons in solids. Nature **583**, 55–59 (2020).
- [36] You, Y. S., Reis, D. A. & Ghimire, S. Anisotropic high-harmonic generation in bulk crystals. Nature Physics **13**, 345–349 (2017).
- [37] Mrudul, M. S., Pattanayak, A., Ivanov, M. & Dixit, G. Direct numerical observation of real-space recollision in high-order harmonic generation from solids. Physical Review A **100**, 043420 (2019).
- [38] Luu, T. T. et al. Extreme ultraviolet high-harmonic spectroscopy of solids. Nature **521**, 498 (2015).
- [39] Lanin, A. A., Stepanov, E. A., Fedotov, A. B. & Zheltikov, A. M. Mapping the electron band structure by intraband high-harmonic generation in solids. Optica **4**, 516–519 (2017).
- [40] Vampa, G. et al. All-optical reconstruction of crystal band structure. Physical Review Letters **115**, 193603 (2015).

- [41] Silva, R. E. F., Blinov, I. V., Rubtsov, A. N., Smirnova, O. & Ivanov, M. High-harmonic spectroscopy of ultrafast many-body dynamics in strongly correlated systems. Nature Photonics **12**, 266 (2018).
- [42] Bauer, D. & Hansen, K. K. High-harmonic generation in solids with and without topological edge states. Physical Review Letters **120**, 177401 (2018).
- [43] Reimann, J. et al. Subcycle observation of lightwave-driven dirac currents in a topological surface band. Nature **562**, 396–400 (2018).
- [44] Garg, M. et al. Multi-petahertz electronic metrology. Nature **538**, 359 (2016).
- [45] Sivis, M. et al. Tailored semiconductors for high-harmonic optoelectronics. Science **357**, 303–306 (2017).
- [46] Mrudul, M. S., Tancogne-Dejean, N., Rubio, A. & Dixit, G. High-harmonic generation from spin-polarised defects in solids. npj Computational Materials **6**, 1–9 (2020).
- [47] Silva, R. E. F., Jiménez-Galán, Á., Amorim, B., Smirnova, O. & Ivanov, M. Topological strong-field physics on sub-laser-cycle timescale. Nature Photonics **13**, 849–854 (2019).
- [48] Reich, S., Maultzsch, J., Thomsen, C. & Ordejon, P. Tight-binding description of graphene. Physical Review B **66**, 035412 (2002).
- [49] Golde, D., Meier, T. & Koch, S. W. High harmonics generated in semiconductor nanostructures by the coupled dynamics of optical inter-and intraband excitations. Physical Review B **77**, 075330 (2008).
- [50] Floss, I. et al. Ab initio multiscale simulation of high-order harmonic generation in solids. Physical Review A **97**, 011401 (2018).
- [51] Hwang, E. H. & Sarma, S. D. Single-particle relaxation time versus transport scattering time in a two-dimensional graphene layer. Physical Review B **77**, 195412 (2008).
- [52] Yoshikawa, N., Tamaya, T. & Tanaka, K. High-harmonic generation in graphene enhanced by elliptically polarized light excitation. Science **356**, 736–738 (2017).
- [53] Heide, C., Higuchi, T., Weber, H. B. & Hommelhoff, P. Coherent electron trajectory control in graphene. Physical review letters **121**, 207401 (2018).
- [54] Higuchi, T., Heide, C., Ullmann, K., Weber, H. B. & Hommelhoff, P. Light-field-driven currents in graphene. Nature **550**, 224 (2017).
- [55] Taucer, M. et al. Nonperturbative harmonic generation in graphene from intense midinfrared pulsed light. Physical Review B **96**, 195420 (2017).

- [56] Liu, C., Zheng, Y., Zeng, Z. & Li, R. Driving-laser ellipticity dependence of high-order harmonic generation in graphene. Physical Review A **97**, 063412 (2018).
- [57] Al-Naib, I., Sipe, J. E. & Dignam, M. M. High harmonic generation in undoped graphene: Interplay of inter-and intraband dynamics. Physical Review B **90**, 245423 (2014).
- [58] Fleischer, A., Kfir, O., Diskin, T., Sidorenko, P. & Cohen, O. Spin angular momentum and tunable polarization in high-harmonic generation. Nature Photonics **8**, 543–549 (2014).
- [59] Neufeld, O., Podolsky, D. & Cohen, O. Floquet group theory and its application to selection rules in harmonic generation. Nature communications **10**, 1–9 (2019).
- [60] Golub, L. & Tarasenko, S. Valley polarization induced second harmonic generation in graphene. Physical Review B **90**, 201402 (2014).